Available online at www.sciencedirect.com
SCIENCE DIRECT
Cement and Concrete Research 35 (2005) 1566–1576
Cement and Concrete Research

# Estimation of air void and aggregate spatial distributions in concrete under uniaxial compression using computer tomography scanning

R.C.K. Wong[a,*], K.T. Chau[b]

[a]Department of Civil Engineering, The University of Calgary, 2500 University Drive NW, Calgary, AB, T2N 1N4 Canada
[b]Department of Civil and Structural Engineering, Hong Kong Polytechnic University, Hong Kong, China

Received 29 March 2004; accepted 25 August 2004

**Abstract**

Normal- and high-strength concrete cylinders (designed compressive strengths of 30 and 90 MPa at 28 days) were loaded uniaxially. Computer tomography (CT) scanning technique was used to examine the evolution of air voids inside the specimens at various loading states up to 85% of the ultimate compressive strength. The normal-strength concrete yielded a very different behaviour in changes of internal microstructure as compared to the high-strength concrete. There were significant instances of nucleation and growth in air voids in the normal-strength concrete specimen, while the increase in air voids in the high-strength concrete specimen was insignificant. In addition, CT images were used for mapping the aggregate spatial distributions within the specimens. No intrinsic anisotropy was detected from the fabric analysis.


*Keywords:* Concrete; High-performance concrete; Pore size distribution; Elastic moduli; Micromechanics

## 1. Introduction

Freeze–thaw action induces cyclic changes in concrete volume resulting in spalling, scaling, and cracking. Air entrainment can enhance the durability of concrete. It results in increased protection against frost action and deicing salt deterioration.

Air exists in concrete in various different forms: aggregate pores, capillary voids, entrained air bubbles, entrapped air voids, and fractures [1]. Aggregate pores are of submicroscopical dimensions and exist within particles of aggregate. These voids do not contribute to the durability of concrete. Capillary voids represent the space not filled by the solid components of the hydrated cement paste. In well-hydrated, low water/cement ratio pastes, the capillary voids may range from 10 to 50 nm; in high water/cement ratio pastes, at early ages of hydration, the capillary voids may be as large as 3 to 5 μm. Entrained air bubbles of 0.05 to 1 mm in diameter can be introduced in concrete by adding small amounts of air-entraining agents. These spherical bubbles are well spaced in the hydrated cement paste to resist damage due to frost action. To ensure adequate frost protection, the spacing factor should not exceed 0.2 mm [2]. The spacing factor is defined as the average maximum distance from any point in the paste to the edge of a void. The smaller the spacing factor, the more durable the concrete is. Large entrapped air voids from 1 to 4 mm can be formed during compaction and casting. Microcracks and fractures can be induced when the concrete is subjected to loading or drying.

There are several standard methods for determination of air void content in freshly mixed and hardened concrete specimens. Gravimetric (ASTM-C138, [3]), volumetric (ASTM-C173, [3]), and pressure (ASTM-C231, [3]) methods can be used to determine the average air content of freshly mixed concrete. However, these three methods do not provide information on the air void size and spatial

* Corresponding author. Tel.: +1 403 220 4998; fax: +1 403 282 7026.
*E-mail address:* rckwong@ucalgary.ca (R.C.K. Wong).

0008-8846/$ - see front matter © 2004 Elsevier Ltd. All rights reserved.
doi:10.1016/j.cemconres.2004.08.016

Table 1
Design mixes of the normal strength (30 MPa) and high strength (90 MPa) concrete

| Content | 30-MPa strength | 90-MPa strength |
|---|---|---|
| Cement (kg/m$^3$) | 300 | 500 |
| Water (kg/m$^3$) | 195 (w/c=0.65) | 130 (w/c=0.24) |
| Sand (kg/m$^3$) | 870 | 660 |
| Aggregates (kg/m$^3$) | 1085 | 1100 |
| Silica fume (kg/m$^3$) | nil | 51 |
| Superplasticer (kg/m$^3$) | nil | 15 |

distributions. The microscopical determination method (ASTM-C457, [3]) can be used to measure dimensions, specific surface, spacing factor, and air/paste ratio of the air–void system in hardened concrete. These spatial parameters are determined based on examination along a series of regularly spaced lines traversed on finely ground sections of hardened concrete. A sufficient number of sections must be taken to reduce the statistical uncertainty.

This paper aims at illustrating that computer tomography (CT) could be a viable, nondestructive method of estimating the air content of hardened concrete. The method offers a 3-D spatial scan of the entire concrete specimen. Continual scanning can be conducted to allow determination of the evolution of air voids under sustained loading. Strength and deformability determined from standard compression tests are overall responses of the test specimens subjected to special testing boundary conditions, and are significantly influenced by the formation of internal fracture and localized shear deformation. It is of importance to correlate the global average deformation behaviour to the local microstructural deformation. The CT scanning quantifies the evolution of the air voids in concrete specimens under uniaxial loading. Results from this study may be useful in interpreting how the fracture mechanism plays a role in governing the compressive strength.

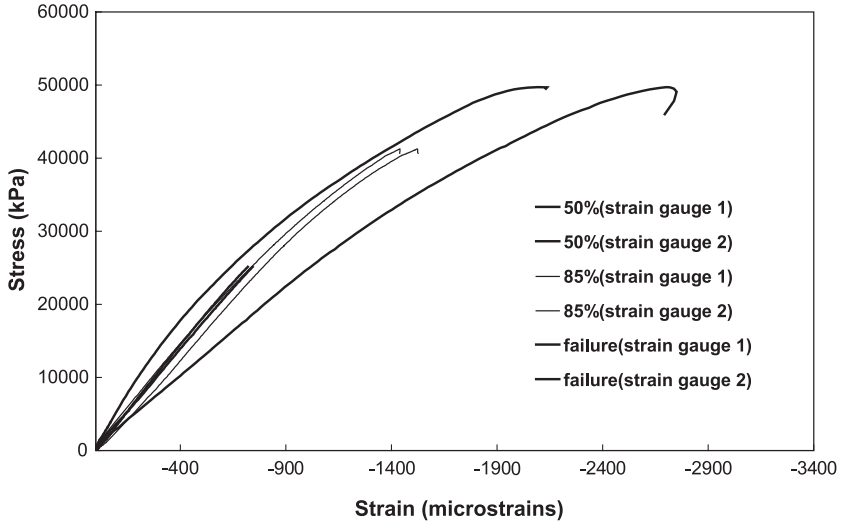


Fig. 1. Stress–strain responses of the 30-MPa concrete specimen under uniaxial compression.

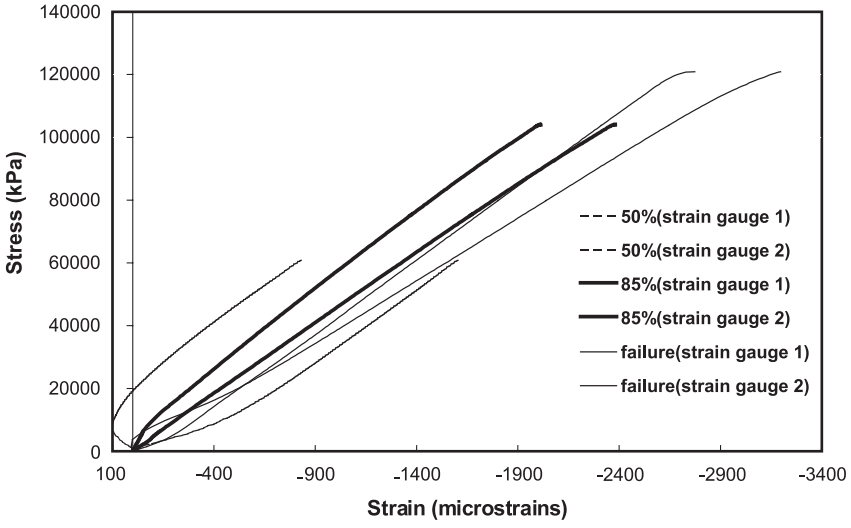


Fig. 2. Stress–strain responses of the 90-MPa concrete specimen under uniaxial compression.

## 2. Experimental technique

Concrete cylinders of 100 mm in diameter and 200 mm in length were cast from two separate batches. The average air contents of the cylinders were determined using the pressure (ASTM-C231) method. Table 1 summarizes the design mixes of the two batches. The cylindrical specimens were cured in a moist room for 15 months. Then, unconfined compression tests were conducted on three specimens from each batch to estimate the average ultimate strength. One specimen from each batch was examined using a computer tomography (CT) scanner. After the CT scanning, two sets of electrical resistance strain gauges were mounted on the specimens to monitor the axial strains under axial loading. The specimens were placed inside a high-capacity load frame, and loaded to 50% of their estimated ultimate strength. Then, the specimens were dismounted from the loading frame, and CT scanned in the unloaded state. The above procedures were repeated with the specimens loaded up to 85% of their estimated ultimate strength. Then, the specimens were loaded to failure.

## 3. Data collection

### 3.1. Stress–strain responses in uniaxial compression tests

Figs. 1 and 2 show the stress–strain responses of the designed 30- and 90-MPa specimens loaded up to 50% and 85% of the estimated ultimate strength, and then to failure in uniaxial compression, respectively.

The 30-MPa specimen exhibited a linear stress–strain with a slope of 36 GPa when it was loaded up to 50% of the estimated ultimate strength. Upon unloading and reloading to 85%, the specimen showed some nonlinearity, indicating occurrence of some plastic deformation. The two-strain gauges gave different responses that might be due to eccentric loading. The specimen failed at an ultimate compressive strength of 50 MPa, at an average overall axial strain of 2%. The 90-MPa specimen exhibited less nonlinearity than the 30-MPa specimen. No nonlinearity was detected even upon loading up to 85% of the ultimate strength. Nonlinearity commenced at about 98% of the ultimate strength. The ultimate compressive strength was 120 MPa at an axial strain of 2.9%, with an average Young's modulus of 43 GPa. The high-strength specimen behaved in a more brittle fashion than the normal-strength specimen.

### 3.2. Computer tomography (CT) scan data

CT imaging has been used to quantify the shear deformation and fracture features of soil samples (e.g., Leung et al. [4], Desrues et al. [5], and Wong [6]). The principles and equipment details of a CT scanner can be found in the above-mentioned references. Only a brief description will be presented herein. The CT scanner used in this study is General Electric Model Hi Speed CT/i. The settings were: 120 kV (KVP), 150 mA (X-ray tube current), 0.8-s full-rotation scan, and 25 cm FOV (field of view). The resolution of each pixel (picture element) was 0.25 mm×0.25 mm×3 mm. The concrete specimen was positioned inside a motorized aluminum tube which slides along the axis of the scanning ring in the CT unit. During the CT scanning process, an X-ray source and an array of detectors rotate in synchrony around the longitudinal axis of the specimen. A multiple set of data is generated from a number of views around a section of the specimen forming a cross-sectional matrix or a scan. More precisely, the X-ray attenuation obtained from different angular positions are combined to generate the pixels (picture element) of the matrix. Each individual pixel represents a specific CT number or a specific X-ray

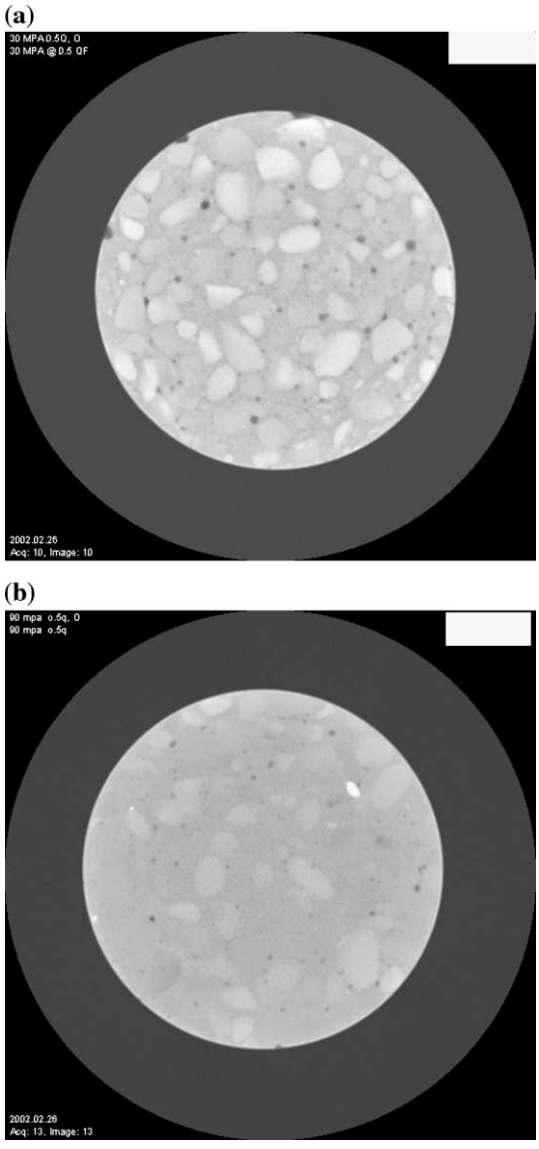


Fig. 3. Computer tomography scans of (a) 30- and (b) 90-MPa concrete specimens.

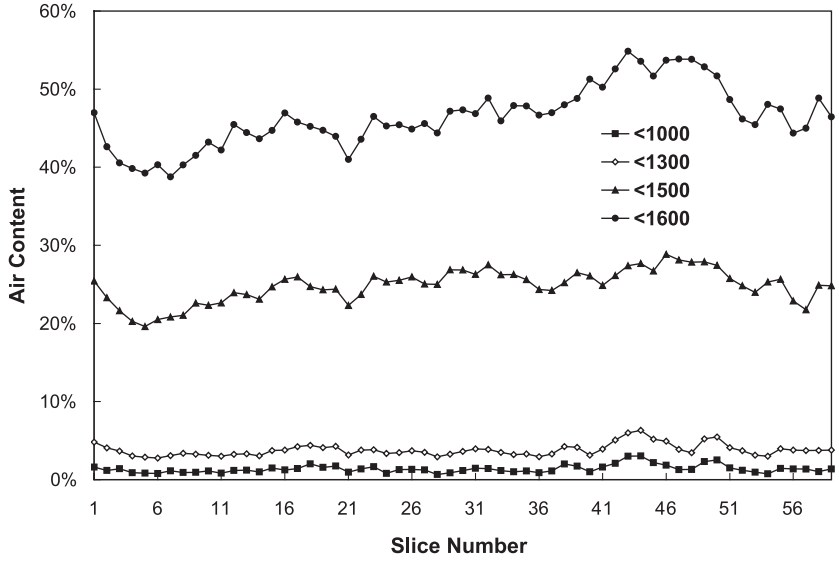


Fig. 4. Sensitivity of threshold CT numbers on estimation of the air content of the 30-MPa concrete specimen (legend shows the CT numbers used in the calibration).

attenuation coefficient normalized with respect to water. Typical CT numbers for the scanned concrete specimens fall in the range of 900–1800. The higher CT number, the denser the material is. Presence of air reduces the CT values. Therefore, the CT number reflects the composition of the pixel containing air, cement, sand, and aggregate.

Each scan is 3-mm thick. Avoiding the edge effects, the scanning started at about 5 mm from the edge of the concrete cylinder. The total number of scans used in this study is about 60. Fig. 3 shows CT images taken at the mid-section of the concrete specimens prior to uniaxial loading. These images were converted from the CT numbers using a graphic software. The light areas represent dense solid aggregates. The dark spots are air voids. It appears that most air void sites were entrained in the sand–cement paste matrix.

## 4. Results and discussion

### 4.1. Air content (void) estimation

The CT scanning is an indirect method which requires calibration of CT scan data with results obtained from direct measurement methods. In addition, the accuracy of

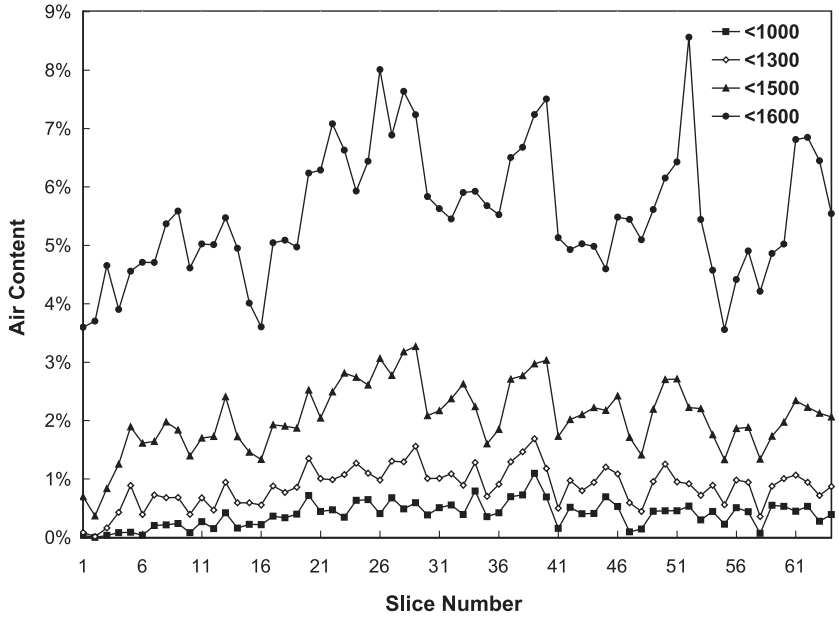


Fig. 5. Sensitivity of threshold CT numbers on estimation of the air content of the 90-MPa concrete specimen (legend shows the CT numbers used in the calibration).

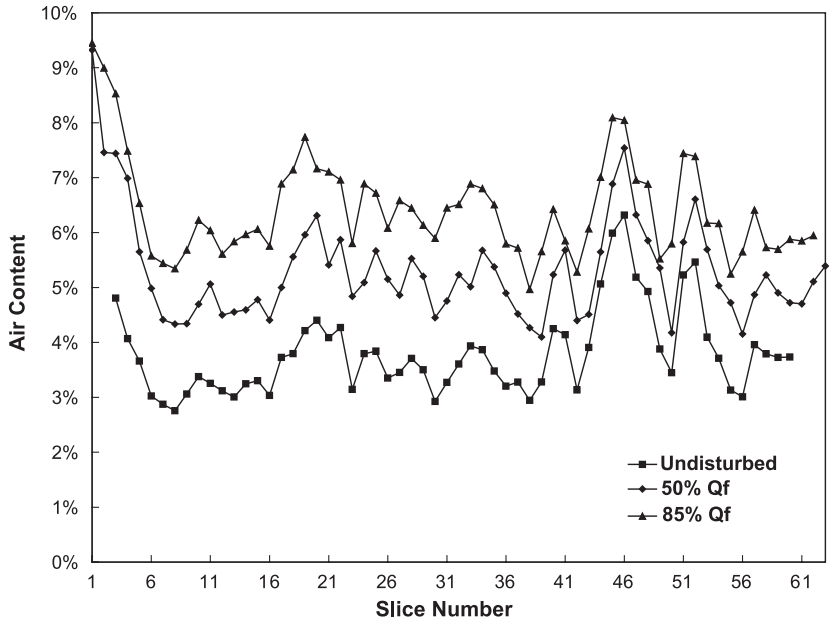


Fig. 6. Air content distribution in the 30-MPa concrete specimen: (■) prior to loading, (◆) loaded to 50% of the ultimate strength, and (▲) loaded to 85% of the ultimate strength.

the method depends on the resolution of the CT scanner, limited by the size of the picture element.

The pressure method (ASTM-C231) was used to determine the air contents of the 30- and 90-MPa concrete specimens. The 30-MPa specimen had an air content of 4.2% that was higher than that of the 90-MPa specimen of 2.1%. No air-entraining agent was added to either mix. This discrepancy in air content between the two specimens is attributed to the fact that the high-strength concrete specimen had a lower water/cement ratio and silica fume (supplementary cementing material) was dosed in the mix. The use of silica fume in blended cement pastes reduces the pore sizes significantly [7]. The major (more than 50%) and dominant pore sizes lie in the range of 500–1000 A (0.05–0.1 μm).

It is obvious that the calibration and interpretation of the raw CT data is dependent on the values chosen for air content. In order to investigate the effect of the chosen parameters on the air content estimation, a sensitivity analysis was conducted. The overall air content measured from the pressure method (ASTM-C231) was compared to those calibrated with CT data. Figs. 4 and 5 present the results of the sensitivity study for the 30- and 90-MPa specimens, respectively. CT numbers of 1300 and 1500 provide good agreement between the CT and pressure measurement methods for the 30- and 90-MPa specimens,

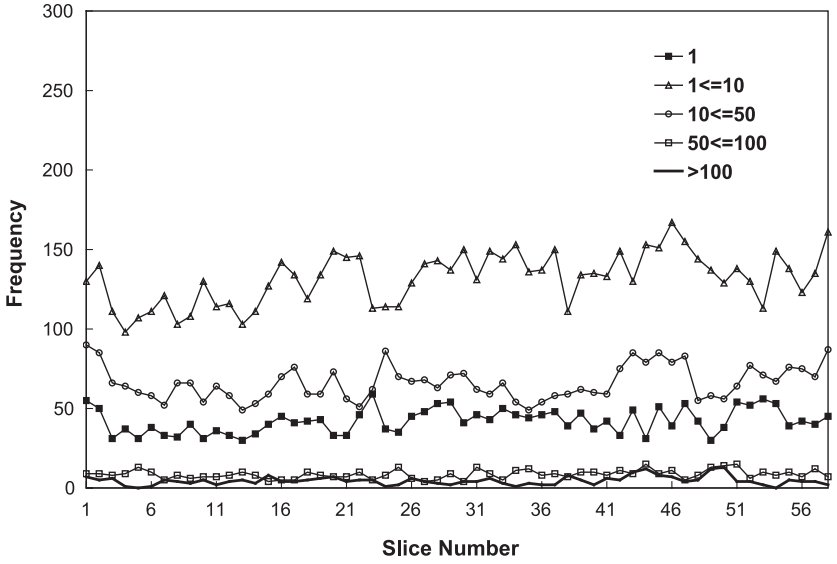


Fig. 7. Air void population in the 30-MPa concrete specimen prior to loading (legend shows the pixel ranges listed in Table 2).

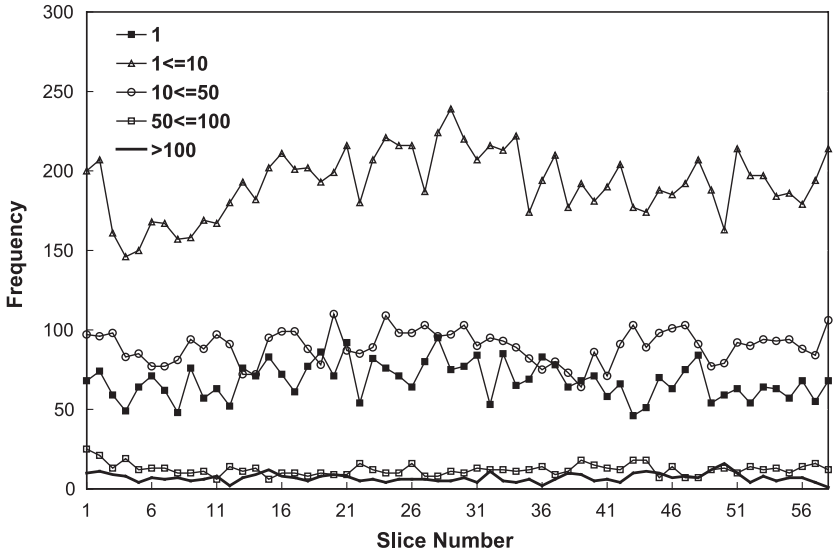


Fig. 8. Air void population in the 30-MPa concrete specimen loaded to 50% of ultimate strength (legend shows the pixel ranges listed in Table 2).

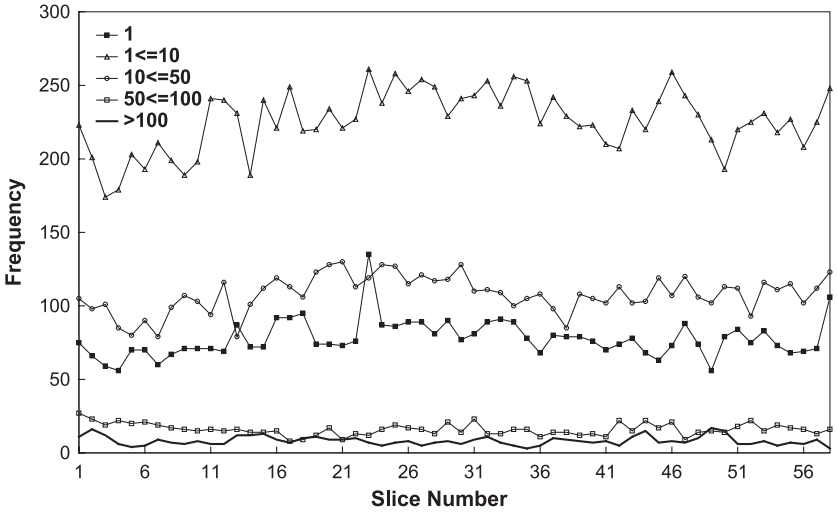


Fig. 9. Air void population in the 30-MPa concrete specimen loaded to 85% of ultimate strength (legend shows the pixel ranges listed in Table 2).

respectively. The calibrated results of the 30-MPa specimen are more sensitive than those of the 90-MPa specimen. The difference in the threshold and sensitivity of the CT numbers between the two specimens may be because the 90-MPa specimen had a slightly higher bulk density than the 30-MPa specimen. The higher the density, the higher the CT number is.

It is important to distinguish how the pressure and CT methods measure the air content of the concrete specimens. The pressure method determines the air content from the change in the volume of the freshly prepared concrete due to a change in the applied pressure. This measured air content includes most collapsible air voids dispersed in the cement paste, but not the micropores in

Table 2
Numbers of air voids detected at various loading states

| Pixels | Void size ($mm^2$) | 30 MPa | | | 90 MPa | | |
|---|---|---|---|---|---|---|---|
| | | Initial | 50% | 85% | Initial | 50% | 80% |
| 1 | 0.25 | 46 | 65 | 73 | 28 | 28 | 29 |
| >1–10 | >0.25–0.79 | 134 | 174 | 227 | 76 | 77 | 77 |
| >10–50 | >0.79–1.77 | 59 | 89 | 110 | 32 | 33 | 33 |
| >50–100 | >1.77–2.50 | 8 | 10 | 15 | 3 | 3 | 4 |
| >100 | >2.50 | 5 | 6 | 6 | 2 | 3 | 3 |

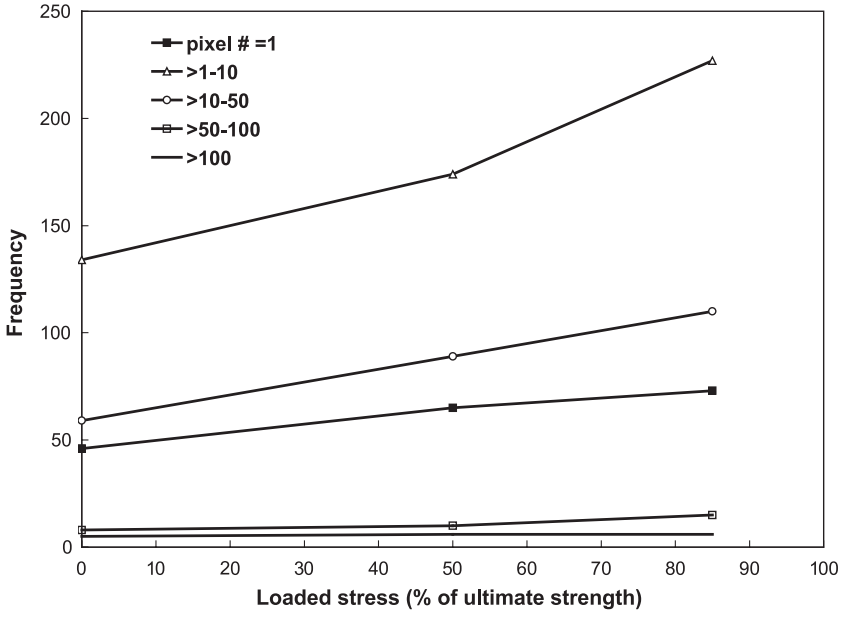


Fig. 10. Frequency of air voids versus loaded stress for 30-MPa concrete specimen (legend shows the pixel ranges listed in Table 2).

the aggregates. Because the CT method is based on the principle of density contrast, this method should detect any air void or space within the concrete. The pixel size used in this study was smaller than that of the spacing factor of the entrained air voids. Thus, the CT methods calibrated with the air content values determined from the pressure method should provide an estimation of the air content contributed mainly from the entrained and entrapped air voids. Micropores and capillary pores were too small to produce a sufficiently large density contrast shown by the CT pixel. The performance of the CT method would be improved if the pixel size was reduced.

### 4.2. Evolution of air void under uniaxial loading

Fig. 6 shows the air content distribution along the specimen length for the 30-MPa specimen under various stages of loading when the threshold CT number of 1300 was used. The detailed populations of the air voids of varying pore sizes are presented in Figs. 7–9 at three loading stages. The air voids were divided into five groups

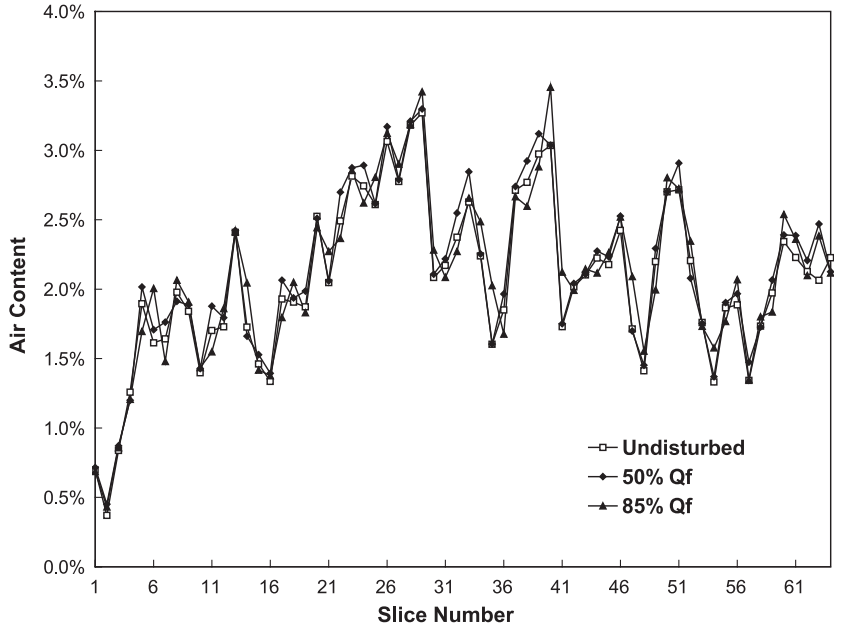


Fig. 11. Air content distribution in the 90-MPa concrete specimen: (□) prior to loading, (◆) loaded to 50% of the ultimate strength, and (▲) loaded to 85% of the ultimate strength.

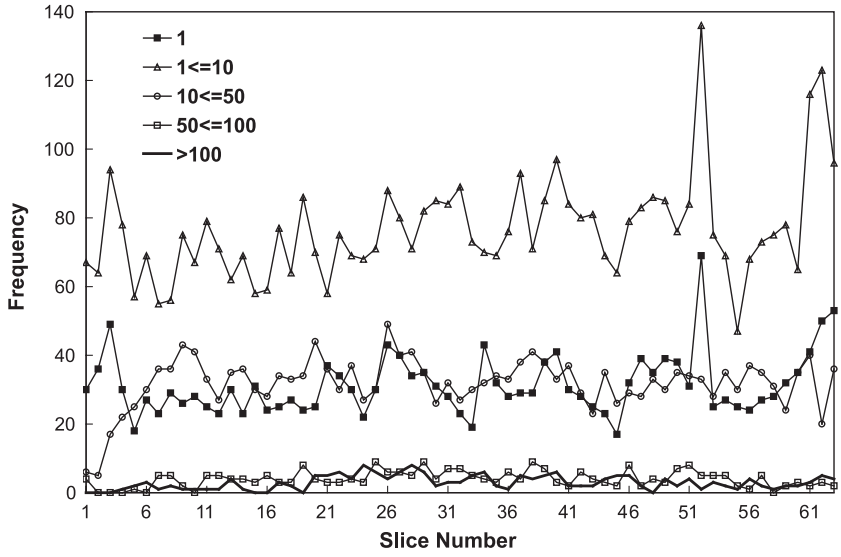


Fig. 12. Air void population in the 90-MPa concrete specimen prior to loading (legend shows the pixel ranges listed in Table 2).

according to their sizes (Table 2). Several features are observed as follows:

(1) The air content is fairly uniformly distributed along the specimen length (Fig. 6), except at two locations (slice numbers 1 and 46; each slice is 3-mm thick).
(2) The dominating air void group is in the range of 0.25–0.79 mm$^2$ (Table 2 and Fig. 7). This group occupies about 53% of the total void frequency. This void size group affects not only the durability of the concrete but also the strength (Mindess and Young 1981; pp. 179 [2]). The compressive strength of the concrete decreases with increasing air content. The durability factor increases to an optimum value with air content increasing from 1% to 7%, and starts to decrease thereafter.
(3) The increase in the average air content at each slice is consistent up to 85% of loading (Fig. 9). This homogenous behaviour implies that no localized deformation was induced due to the shear loading.
(4) Each air void group has a different increasing rate upon loading. The increasing rate may be due to new nucleation or growth or to microcracking. The air void group of 0.25–0.79 mm$^2$ has the highest increase rate (Fig. 10) as compared to the other groups. In addition, the increase rate of this group becomes larger or nonlinear from 50% to 85 % loading whereas the rates of other groups are constant. This nonlinear response explains the non-linear stress-strain relation observed in the uniaxial loading. Total of 92 and 87 new air voids of the smallest size were generated in the load increments

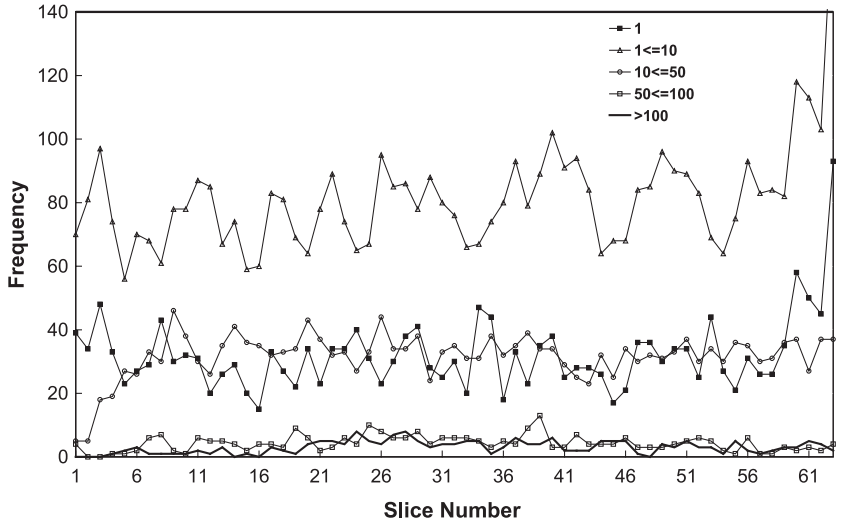


Fig. 13. Air void population in the 90-MPa concrete specimen loaded to 50% of ultimate strength (legend shows the pixel ranges listed in Table 2).

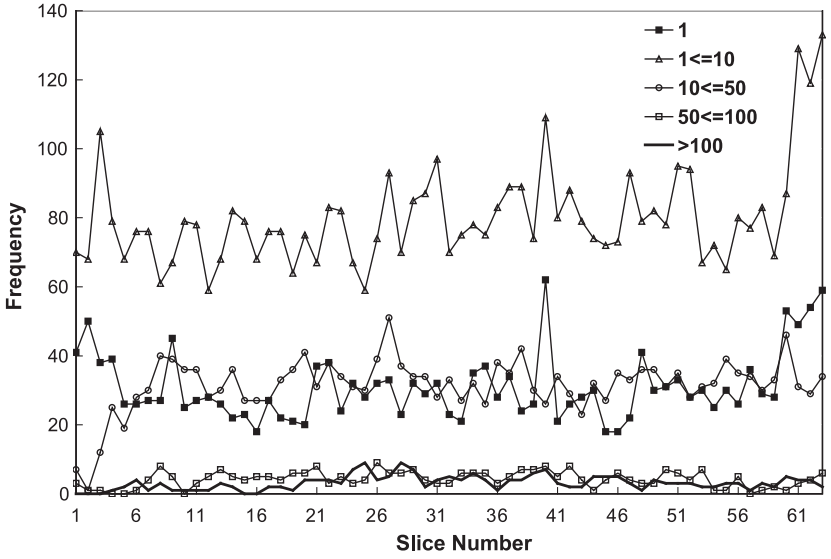


Fig. 14. Air void population in the 90-MPa concrete specimen loaded to 85% of ultimate strength (legend shows the pixel ranges listed in Table 2).

from 0% to 50% and 50% to 85% of the ultimate load, respectively.

(5) There were a few large air voids, and their nucleation or growth rate was small.

For the 90-MPa specimen, the air void group of size of 0.25–0.79 mm$^2$ is also the prominent group (Table 2 and Fig. 11). However, the increase rates in all groups are minimal (Figs. 12–14). This explains why the specimen did not display any nonlinear or plastic deformation in the uniaxial loading. No nucleation and growth rate in each air void range was detected.

Compared to the 30-MPa concrete, the 90-MPa concrete behaves more like a homogeneous material. For the high-strength concrete, the stress–strain curve is steeper and more linear to a higher stress/strength ratio than the normal-strength specimen. Small amount of growth in air void (probably due to microcracking) was detected in the 90-MPa specimen at loading up to 85% of the ultimate strength. This suggests that the high-strength concrete can be loaded to a higher stress/strength ratio without initiating a self-propagating mechanism leading to disruptive failure.

### 4.3. Solid aggregate fabric

Grain fabric refers to as spatial arrangement of particles, particle groups, and pore spaces in a granular medium. The spatial arrangement includes the orientation of the particle's axes, the average number of contact for

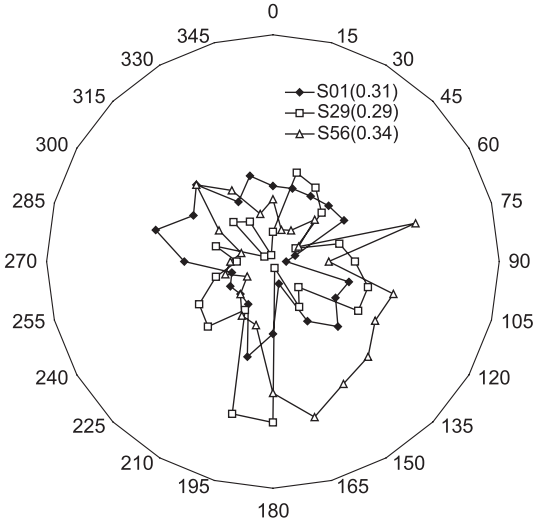


Fig. 15. Rosettes of aggregate fractions of the 30-MPa concrete specimens at different horizontal sections (S01, Section 01; bracketed value=average aggregate fraction).

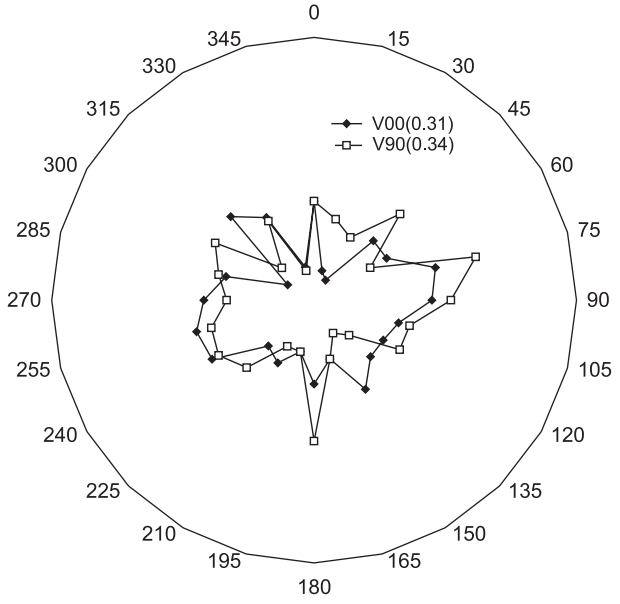


Fig. 16. Rosettes of aggregate fractions of the 30-MPa concrete specimens at two vertical sections (bracketed value=average aggregate fraction).

each particle, the distribution of the contact normal, and the distribution of voids.

Muhunthan and Chameau [8] proposed the use of a fabric tensor based on void space to characterize the fabric of soils. This approach was adapted to detect any intrinsic fabric anisotropy of aggregates in the 30- and 90-MPa concrete specimens during placement and compaction. A fabric tensor based on solid aggregate fraction instead of void fraction was used. This technique involved laying a set of radial probe lines drawn at 10° intervals on the CT scans of the concrete specimen. The total length of the interceptions of the solid aggregates on each test ray was measured, and divided by the length of the probe line yielding the solid fraction. The above evaluation was conducted on three horizontal sections and was repeated for two perpendicular vertical sections. The vertical sections were prepared by staggering the 2-D horizontal CT scans. Figs. 15 and 16 show the polar distributions of the solid fraction for horizontal and vertical sections of the 30-MPa specimen, respectively. There is no preferred orientation in solid fraction or aggregate arrangement. For the 30-MPa specimen, the aggregate fraction varies from 0.26 to 0.38 and from 0.31 to 0.34 in horizontal and vertical sections, respectively. The solid fraction estimated from the design mix is 0.41 based on aggregates. It should be noted that the solid fraction tensor provides an indicator of aggregate packing and is not representative of the average aggregate fraction of the concrete specimen. To estimate the average aggregate fraction, the microscopical determination method (ASTM-C457) based on the equally spaced traverse lines should be used.

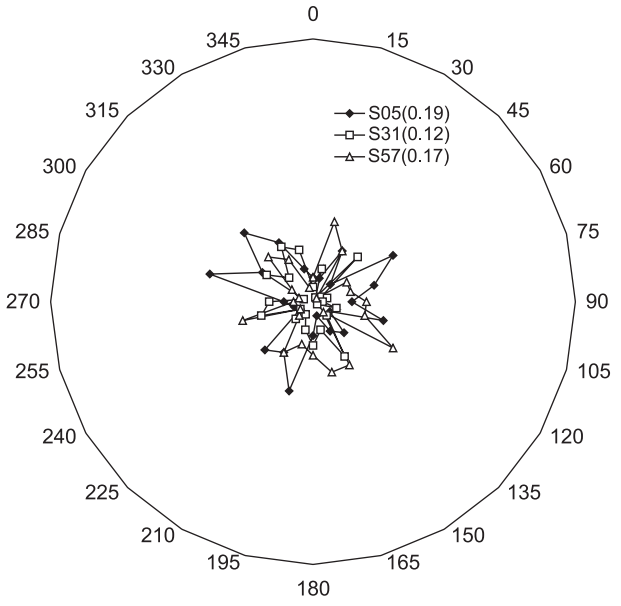


Fig. 17. Rosettes of aggregate fractions of the 90-MPa concrete specimens at different horizontal sections (S05, Section 05; bracketed value=average aggregate fraction).

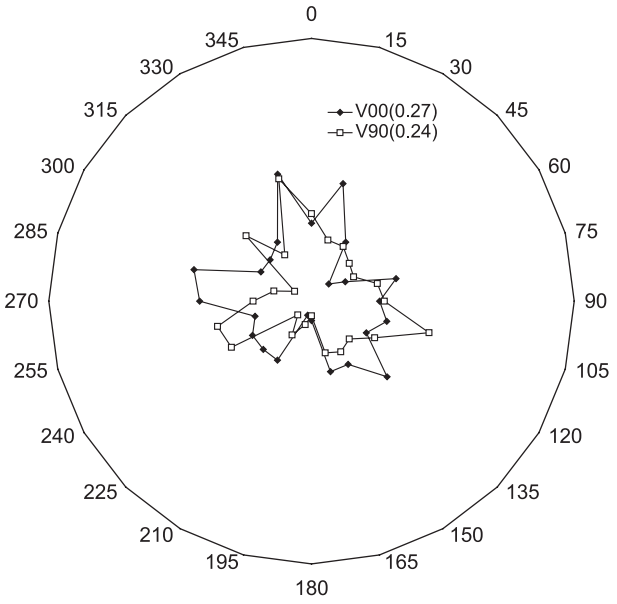


Fig. 18. Rosettes of aggregate fractions of the 90-MPa concrete specimens at two vertical sections (bracketed value=average aggregate fraction).

For the 90-MPa specimen, the aggregate fraction varies from 0.12 to 0.26 and from 0.24 to 0.27 in horizontal and vertical sections, respectively (Figs. 17 and 18). The solid fraction estimated from the design mix is 0.41 based on aggregates. The high cement content might mask some aggregates making the concrete more homogeneous. In the 30-MPa concrete specimen, more water (65 g) and less cement (200 g) replaced by the sand were used.

## 5. Conclusion

The experimental findings from this research investigation have verified that computer tomography technique could be used as a nondestructive analytical tool to determine the spatial distributions of the air voids and aggregate fabric in hardened concrete specimens. Evolution of air voids in the normal (30 MPa) and high strength (90 MPa) under uniaxial compression loading were different. For the normal-strength concrete, significant nucleation and growth in air voids due to loading were detected in the air voids of sizes of 0.25 $mm^2$. However, there was no such observation in high-strength concrete specimens loaded up to 85% of the ultimate strength. No intrinsic anisotropy in aggregate spatial distribution of both concrete mixes was detected from the fabric analysis.

## Acknowledgement

This study was made possible under collaboration between University of Calgary and Hong Kong Polytechnic University. Financial supports from PolyU Project No. GT-213 are appreciated. Peter Thomson (on NSERC Post-

Graduate Scholarship) and Alex Cheung (on NSERC Undergraduate Research Award) conducted part of CT data analysis.

## References

[1] P.K. Mehta, P.J.M. Monteiro, Concrete: Structure, Properties, and Materials, Prentice Hall, Englewood Cliffs, New Jersey, 1991, pp. 28–29.
[2] S. Mindess, J.F. Young, Concrete, Prentice Hall, Englewood Cliffs, New Jersey, 1981, pp. 172–174.
[3] ASTM. Volume 04.02 Concrete and Aggregates, American Society for Testing and Materials, 1998.
[4] S.K. Leung, P.R. Kry, R.C.K. Wong, Visualization of deformation in unconsolidated Athabasca oil sand, International Heavy Oil Symposium, Society of Petroleum Engineers, Calgary, Alberta, Canada, June 18–21, 1995, SPE 30315.
[5] J. Desrues, R. Chambon, M. Mokni, F. Mazerolle, Void ratio evolution inside shear bands in triaxial sand specimens studied by computed tomography, Geotechnique 46 (1996) 529–546.
[6] R.C.K. Wong, Shear deformation of locked sand in triaxial compression, Journal of Geotechnical Testing 23 (2000) 158–170.
[7] R.C.K. Wong, J.E. Gillott, J.E., S. Law, M.J. Thomas, C.S. Poon, Calcined oil sands fine tailings as a supplementary cementing material for concrete, Cement and Concrete Research, 34 (7) 1235–1242.
[8] B. Muhunthan, J.L. Chameau, Void fabric tensor and ultimate state surface of soils, Journal of Geotechnical and Geoenvironmental Engineering 123 (1997) 173–180.